Research Article | Vol. 34, No. 17 / 24 Aug 2026 / Optics Express 32265
Optics EXPRESS

Multifunctional tunable on-chip meta-waveguides enabled via liquid crystals

WENYONG XIE,[1,2,3] AVIAD KATIYI,[4] ALINA KARABCHEVSKY,[4,5] ATEFEH HABIBPOURMOGHADAM,[1,2,3,*] AND ANTONIO CALÀ LESINA[1,2,3]

[1] *Institute of Photonic Systems and Technologies, Leibniz University Hannover, Hannover, 30167, Germany*
[2] *Hannover Centre for Optical Technologies, Leibniz University Hannover, Hannover, 30167, Germany*
[3] *Cluster of Excellence PhoenixD, Leibniz University Hannover, Hannover, 30167, Germany*
[4] *School of Electrical and Computer Engineering, Ben-Gurion University of the Negev, Beer-Sheva 8410501, Israel*
[5] *Department of Physics, Lancaster University, LA1 4YB, United Kingdom*
[*] *atefeh.habibpoor@hot.uni-hannover.de*

Abstract: Meta-waveguides combine traditional waveguides with metamaterials concepts to achieve unprecedented control of guided light. This can be obtained through subwavelength structural engineering of the waveguide itself or via metasurfaces integrated with the waveguide. An active research direction is the reprogrammability of such systems, with several techniques already explored for single-function devices. However, a compact solution that can control multiple light properties (i.e., phase, intensity, and polarization) has not been reported. Here, we introduce what we believe is a new class of electrically reconfigurable on-chip meta-waveguides enabled by the incorporation of liquid crystals (LCs). We first investigate the proposed devices using the widely adopted approximation of a spatially uniform anisotropic LC medium, providing an insightful framework for device design and performance estimation. To bridge the gap toward experimental implementation, we subsequently employ a Q-tensor model to address the infiltration constraints into the structured meta-waveguides. This method can capture voltage-driven spatial variations of the LC director, including elastic deformations, surface anchoring, defect formation, and electrode-induced reorientation. This comparison provide a reliable guide on how to initially define LC profile inside each device to achieve a target performance. We propose and numerically demonstrate two architectures: LC-integrated 1D- and 2D-Bragg meta-waveguides on a silicon platform that overcome the limitations of conventional passive meta-waveguides and enable multifunctional optical control. The 1D design achieves high-contrast intensity modulation for both fundamental TE and TM modes, continuous polarization conversion with 81.86% efficiency, and π level phase shifts with low insertion loss over the respective wavelength ranges. The 2D design further enhances compactness, enabling low-loss π phase modulation and broadband intensity control within an ultra-compact 3.3 µm footprint. Our findings identify a compact platform for electrically tunable LC-integrated 1D- and 2D-Bragg meta-waveguides offering a promising route toward densely reprogrammable photonic circuits.

1. Introduction

The rapid scientific progress on nanostructured and meta-photonic devices is significantly impacting the field of integrated optics. By tailoring light–matter interactions at the nanoscale, these structures enable compact and multifunctional optical elements directly on a chip, tremendously expanding the design space and functionalities of conventional waveguide platforms [1]. This is achieved through several design architectures, including integrated metasurfaces [2,3],

#605472 https://doi.org/10.1364/OE.605472
Journal © 2026 Received 15 Jun 2026; revised 4 Aug 2026; accepted 4 Aug 2026; published 18 Aug 2026

subwavelength-nanostructured waveguides [4–6], metasurfaces on the top surface [7] or on the facet of waveguides [8], and complex designs enabled by advanced optimization and inverse design algorithms [9]. Throughout this paper, we collectively refer to all these architectures as meta-waveguides [10].

While traditional passive meta-waveguides exhibit a fixed optical response once fabricated, there is a growing interest in their post-fabrication dynamic tuning to enable a wide variety of applications. This includes high-speed modulators [11], logic gates for reconfigurable optical computing [12], dynamic beam shaping and wavefront control [13], tunable single-photon sources [14], and emerging building blocks for integrated optical computing such as reconfigurable linear operators for matrix operations [15], reprogrammable photonic processors [16], and integrated photonic nonlinear activation functions for optical neural networks [17].

Among the various tuning strategies for meta-photonics applicable on-chip, there are mechanical stretching [10,18], phase change materials [19,20], electro-optic effects [21], and LCs [22–30]. These techniques modulate the refractive index locally, which in turn can be exploited for optical reconfigurability. For example, widely used strategies include the electro-optic effect in lithium niobate [31–34] and barium titanate [35], Kerr electro-optic effect [36], and free-carrier dispersion, where carrier injection, accumulation, or depletion can enable high-speed refractive index control [37,38]. However, the key building blocks of photonic integrated circuits (PICs), such as dynamic phase shifters, optical switches [39], and polarization converters [40,41], are still limited in terms of efficiency and footprint [10,42].

Existing phase shifters mainly modulate the effective refractive index through micro-electro-mechanical systems (MEMS), thermo-optic effect, free-carrier dispersion, or phase-change materials (PCMs) [43]. Phase shifters based on free-carrier dispersion typically have lengths ranging from hundreds of microns to one millimeter [44]. At the same time, PCM-based devices suffer from additional optical losses of approximately 25 dB/cm and require footprints of several tens of microns [45]. MEMS-based phase shifters offer ultra-low power consumption and compactness but face fabrication complexity and potential mechanical fatigue [46]. As a key figure of merit for phase modulators, $V_\pi L_\pi$ (i.e., the voltage multiplied by length to achieve a π phase shift) of typical devices usually lies in the range of several volts times several hundreds of micrometers to several millimeters [47–50].

For optical switching, micro-ring resonator (MRR) and Mach–Zehnder interferometer (MZI) configurations have been widely explored [51,52]. They often suffer from large footprint, crosstalk, and high power consumption [51]. Several representative MRR- and MZI-based optical switches typically require footprints ranging from several tens of micrometers to several millimeters, with insertion losses spanning from approximately 0.9 dB to 9.6 dB [53–55].

Polarization modulators operating near communication wavelengths typically exhibit lateral footprints in the range of several tens to hundreds of micrometers, with polarization extinction ratio (ER) values ranging from 12 dB to 31.9 dB [56–58]. Polarization rotation in these devices is usually enabled by waveguide cross-section engineering. Utilizing meta-waveguides is also a feasible approach, as a 1D chain of high-index dielectric cylinders can serve as a passive waveplate for guided-wave polarization control [59]. Although these devices can achieve high polarization ER, the polarization control remains passive. Continuous polarization rotation enables the generation of arbitrary polarization states. The key is the ability to control the polarization ER, thereby enabling arbitrary polarization states via mixing of TE and TM modes. Several approaches have been reported, for example by controlling structural anisotropy using PCM [60] or MEMS [61] to realize this functionality.

The functionalities described above in PIC technology are typically achieved in single-function devices, which often suffer from limited tunability and large footprints. In order to overcome these limitations, we propose LC-integrated meta-waveguides on silicon-on-insulator platforms. The incorporation of LCs provides multiple advantages, such as electrically reconfigurable anisotropy, high electrical sensitivity, relatively large birefringence [62], and modulation speeds reaching the MHz regime [27,63], and even up to the GHz regime for ferroelectric LCs [64] (in contrast to the typically kHz-level response of non-ferroelectric LCs). Nevertheless, the combination of LCs with nanostructured waveguides is still in its infancy. In Ref. [65], optical switching is demonstrated in LC-integrated meta-waveguides, achieving a 16 dB switching ratio at 1550 nm. In Ref. [66], the concept was applied to achieve phase shifting in MZIs and MRRs, enabling a 2π phase shift control. However, polarization tuning and the modulation of TM-polarized guided modes have not yet been explored. Low-power and fast thermo-optic switching has also been demonstrated in a nematic LC-filled silicon slot-waveguide directional coupler, highlighting the potential of LC-integrated silicon photonics for energy-efficient reconfigurable devices [27]. Additionally, electrically tuning the LC alignment in an electro-optic directional coupler integrated with LC enabled an ultralow $V_{\pi}L$ switch at 1550 nm [28].

In this work, we introduce two types of modulators based on one-dimentional (1D)- and two-dimensional (2D)-Bragg structures infiltrated with LCs. We demonstrate phase, intensity, and polarization modulation of guided modes in each LC-integrated meta-waveguide over their respective operating wavelength ranges. The proposed 1D- and 2D-Bragg designs also exhibit low propagation loss in the near-infrared regime, making them suitable for large-scale PICs. The 1D-Bragg structure is built from identical grooves made into the Si waveguide, while the 2D-Bragg structure is formed from an etched elliptical pillar array on a silicon rib waveguide. By means of the particle swarm optimization (PSO) algorithm (implemented in Ansys Lumerical), the final geometrical designs are obtained in the presence of LCs.

The proposed meta-waveguides are first analyzed using the widely adopted approximation of a spatially uniform anisotropic LC medium, providing an insightful framework for device design and optimization. We then perform a more physically realistic and experiment-oriented modelling using a Q-tensor model that captures spatially varying LC director distributions under applied voltage, including bulk elastic deformations, surface anchoring, and electrode effects [67–69]. Our findings support the practical feasibility of the proposed structures under realistic, non-uniform LC distributions. Moreover, we show that, with appropriate LC material selection, anchoring conditions, and electrodes design, their performances can closely approach those obtained through the implementations of the simplified uniform-LC models. The proposed devices provide a compact platform for reconfigurable integrated photonics, enabling phase, intensity, and polarization modulation through electrically controlled LC configurations over their respective operating wavelength ranges.

In Sec. 2.1, we discuss how the nanostructured waveguides based on a 1D-Bragg structure manipulate the photonic bandgap through LC infiltration to control intensity and phase. In Sec. 2.2, we further show that the reorientation of LCs within the waveguide cross-sectional plane enables arbitrary mixing of TE and TM modes, achieving arbitrary linear polarization states. In Sec. 2.3, we present a more compact intensity and phase modulator based on a 2D-Bragg structure. In Sec. 3.1, we investigate the influence of the etched surface profile on device performance. In Sec. 3.2, the optical performance of each waveguide under non-uniform LC director-field distributions and voltage-induced reorientation is presented. In Sec. 4.1, we discuss the transfer matrix method and explain how the theory is employed to predesign and analyze the 1D-Bragg structure filled with the anisotropic material for intensity, phase, and polarization modulation. The method for simulating the LC director-field and the underlying physics governing LC reorientation are presented in Sec. 4.2.

2. Results and discussion

2.1. Phase and intensity modulation in 1D-Bragg nanostructured waveguides

On-chip modulators are fundamental components in PICs and are expected to provide effective control over the fundamental properties of guided light beam. In this section, we demonstrate the

Optics EXPRESS

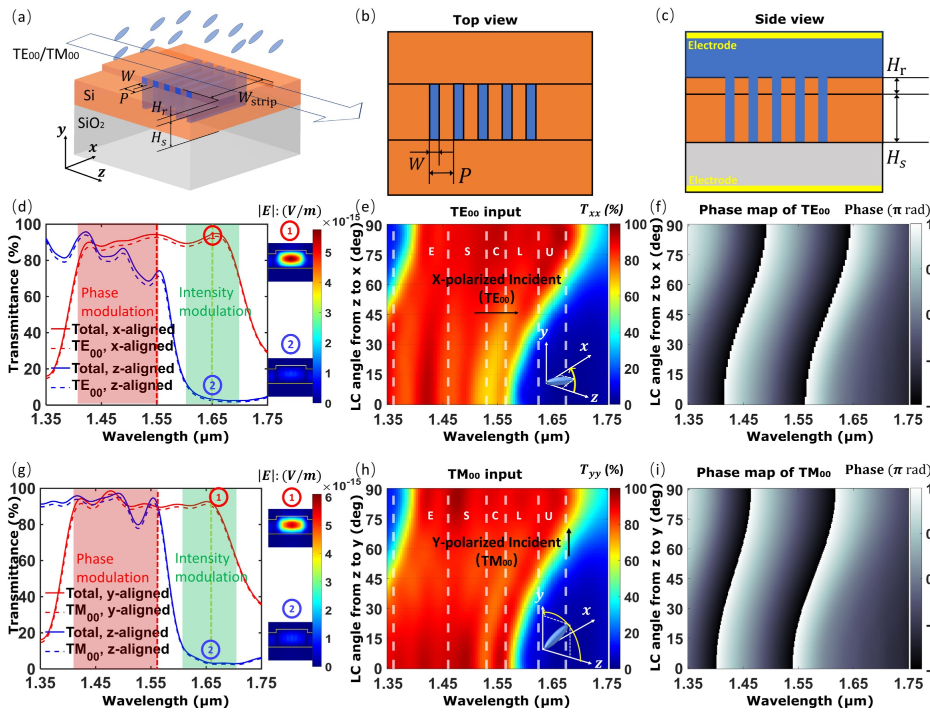

Fig. 1. Schematic and LCs-controlled phase and intensity modulation of the 1D-Bragg Si rib waveguide. (a) Schematic of etched gratings on a silicon rib waveguide. (b) Top-view and (c) side-view showing the electrodes' position. (d) Transmittance spectra under TE_{00} mode excitation for x- and z-aligned LCs states. A phase shift of $\approx 0.92\pi$ occurs at 1.55 μm (red dashed line), and intensity modulation occurs at 1.65 μm (green dashed line). The two output field distributions ($|E|$) on the right correspond to the marked spectral points. (e) Transmittance spectra and (f) phase shift under TE_{00} mode excitation as the LC director-field reorients from the z-axis to the x-axis. (g) Transmittance spectra under TM_{00} mode excitation for y- and z-aligned LCs states. A phase shift of $\approx 0.92\pi$ occurs at 1.55 μm (red dashed line), and intensity modulation occurs at 1.65 μm (green dashed line). The two output field distributions ($|E|$) on the right correspond to the marked spectral points. (h) Transmittance spectra and (i) phase shift under TM_{00} mode excitation as the LC director-field reorients from the z-axis to the y-axis.

first design based on a waveguide nanostructured in 1D and infiltrated with LCs given uniform distributions to evaluate the idealized performance limits of the device. The concept of this device is to introduce periodically LC-infiltrated nanostructures into a silicon rib waveguide to form a Bragg-type modulation region, aimed at modulating the phase, intensity, and polarization of the fundamental TE_{00} and TM_{00} modes (representing the two fundamental eigenmodes with x- and y-polarization), respectively. Although such waveguide designs can support multimode guidance over the wavelength range of interest, mode decomposition shows that the output is dominated by the fundamental modes for all considered LC orientations. We therefore focus on the phase, intensity, and polarization modulation of these two fundamental modes. A spatially non-uniform LC director-field may introduce additional coupling channels to higher-order modes, which will be discussed in Sec. 3.2.

Figure 1(a) schematically depicts the proposed 1D-Bragg grating structure; top and side views are shown in Fig. 1(b,c), respectively. The waveguide is made of Si material and is fabricated on a SiO_2 substrate. This has a stripped structure (with a thickness of $W_{strip} = 10\ \mu m$) made from five

Optics EXPRESS

identical grooves oriented normal to the substrate, fully built into the Si layer and extended up to the strip top surface. The Si slab thickness (H_s) is 1.6 µm, and the vertical rib height measured from the slab surface to the waveguide top (H_r) is 0.4 µm (Fig. 1(c)). The etched regions are assumed filled with BL009 LCs (a cyanobiphenyl mixture from Merck), which exhibit slightly higher refractive indices (n_o = 1.59, n_e = 1.87) [70] and larger birefringence compared to the commonly used E7 nematic LCs. These LC-infiltrated grooves, embedded into the Si waveguide, form a periodic structure analogous to a Bragg grating. By carefully designing the groove width (W) and period (P) (Fig. 1(b)), a photonic bandgap can be positioned at the target operating wavelength and subsequently tuned via electrically driven LCs reorientation. Moreover, the polarization coupling resulting from the off-diagonal permittivity components ϵ_{ij} ($i \neq j$) can be actively tuned by adjusting the LCs orientation. Consequently, as the TE_{00} and TM_{00} guided modes propagate through the periodically LC-infiltrated regions, their transmitted intensity, phase, and polarization can be continuously modulated. The total length of the optimized structure is only 4.3 µm.

To realize the aforementioned functionalities, simulations are performed with the Ansys Lumerical FDTD solver, and the design is optimized with the PSO algorithm in Ansys Lumerical. The optimized groove parameters W = 424 nm and P = 970 nm are obtained to maximize transmittance, mode purity, and polarization conversion. The optimization is set based on two fundamental LCs alignment states, in which LCs alignment is assumed parallel and perpendicular to the substrate plane. In our approach, the initial values of the structural parameters were determined from a pre-designed structure obtained from the application of the transfer matrix method as described in the Methods section, and used to initialize the optimization process. The optimization range was defined by setting upper and lower bounds for each design variable. The population size was set to 10. The optimization targets included the transmittance and mode purity at 1.55 µm and 1.65 µm under the two LC states, with equal weights (= 1) assigned to each objective.

Regarding phase and intensity modulation of the fundamental modes (i.e., TE_{00} and TM_{00}) through controllable LC reorientation, two representative LC orientation states are selected, and the corresponding transmission spectra and output field distributions in the waveguide are presented in Fig. 1(d,g). Specifically, LC reorientation in the xz-plane modulates the TE_{00} mode, while reorientation in the yz-plane enables modulation of the TM_{00} mode. As seen from Fig. 1(d), at 1.55 µm, the phase modulation (of $\approx$ 0.92π) is accompanied by an intensity variation of approximately 15%, while at 1.65 µm, the structure functions solely as a high-contrast optical switch with a switching ratio close to 90%, corresponding to an ER of 14.6 dB, defined as $\mathrm{ER} = 10\log_{10}(T_{\mathrm{on}}/T_{\mathrm{off}})$ [71]. Reorientation of the LCs from y-aligned to z-aligned allows modulation of both the phase and intensity of the TM_{00} mode exclusively, as shown in Fig. 1(g). Again, a high switching contrast of nearly 90% (ER = 13.8 dB) is achieved at 1.65 µm, whereas at 1.55 µm the output intensity remains almost unchanged during phase modulation (of $\approx$ 0.92π), indicating ideal phase shifter behavior. Furthermore, the two output field distributions ($|E|$) shown on the right confirm that the device supports intensity modulation with mode purities exceeding 95%. Considering practical integration issues with CMOS platforms and fiber coupling between photonic chips, as well as the transparency window of silicon starting from 1100 nm, we adopt the commonly used O-, E-, S-, C-, L-, and U-band (OESCLU) classification in the optical wavelength range of 1100–1675 nm covering the standard infrared bands used in optical communication systems and photonic computing, including the extended O-band (1100–1260 nm), O-band (1260–1360 nm), E-band (1360–1460 nm), S-band (1460–1530 nm), C-band (1530–1565 nm), L-band (1565–1625 nm), and U-band (1625–1675 nm), referred to as OESCLU-bands [72,73]. White dashed lines are used in Fig. 1(e,h), Fig. 2, and Fig. 4 to indicate the division.

Although two representative LCs orientation states corresponding to TE_{00} and TM_{00} modulation are presented above for clarity, the LCs orientation in fact can be continuously tuned through

Optics EXPRESS

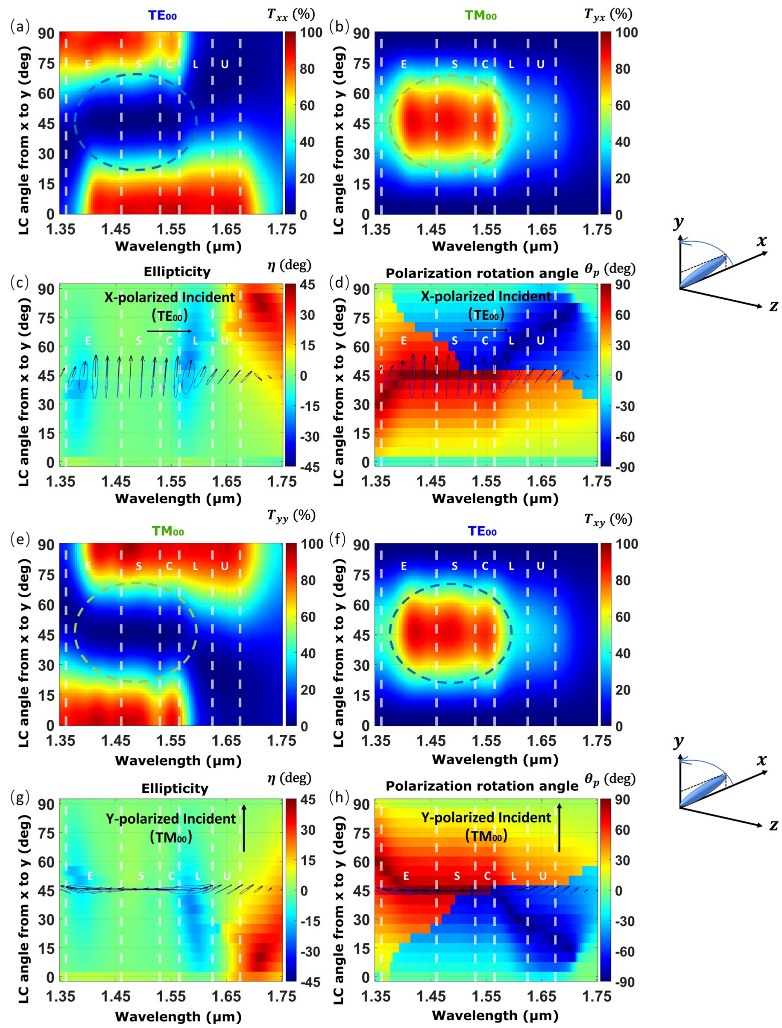

Fig. 2. Polarization modulation and performance evaluation. Optical response under TE_{00} mode excitation with LCs reorientation in the *xy*-plane: (a) co-polarized TE_{00} transmittance T_{xx}, (b) cross-polarized TM_{00} transmittance T_{yx}, (c) ellipticity η, and (d) polarization rotation azimuth angle θ_p. Optical response under TM_{00} mode excitation with LCs reorientation in the *xy*-plane: (e) co-polarized TM_{00} transmittance T_{yy}, (f) cross-polarized TE_{00} transmittance T_{xy}, (g) ellipticity η, and (h) polarization rotation azimuth angle θ_p.

voltage control, enabling continuous modulation of the optical response. Therefore, we further analyze the optical responses of the device under fundamental TE/TM mode excitation as a function of the LCs rotation angle, which intuitively illustrates the dependence of the transmittance spectra with respect to the LCs orientation (Fig. 1(e, h)). Evidently, the passband exhibits a redshift of approximately 0.15 μm with increasing rotation angle. This indicates that power modulation with a bandwidth of up to 0.15 μm can be achieved in the L- and U-bands using the two illustrated LCs reorientation strategies for the TE_{00} and TM_{00} modes, respectively. Moreover, in the wavelength range of 1.4–1.55 μm, the transmittance remains nearly constant, enabling pure phase modulation with a bandwidth of 0.15 μm and a modulation depth reaching up to ≈ 0.92π, as supported by the phase modulation shown in Fig. 1(i, f).

Optics EXPRESS

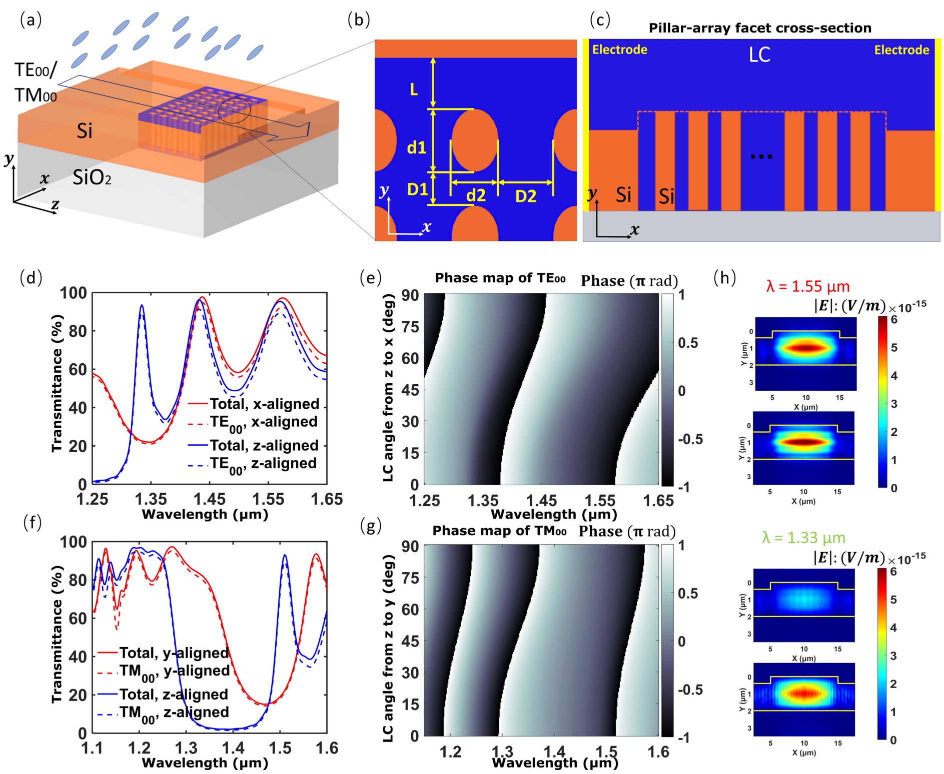

Fig. 3. Schematic and LCs-controlled phase and intensity modulation of the 2D-Bragg Si rib waveguide. (a) Schematic of the etched elliptical pillar array structure on a silicon rib waveguide. (b) Top-view zoom-in of the elliptical pillar array structure. (c) Cross-sectional view. (d) Output transmittance and the corresponding (e) phase variation under TE_{00} mode excitation for the x- and z-aligned LC states. (f) Output transmittance and the corresponding (g) phase variation under TM_{00} mode excitation for the y- and z-aligned LC states. (h) Output field distributions of the TE_{00} mode injection at the operating wavelengths 1.55 μm (upper group) and 1.33 μm (lower group) under the x-aligned (top) and z-aligned (bottom) LCs states.

2.2. Polarization modulation in 1D-Bragg nanostructured waveguides

In common silicon-on-insulator waveguides with structural anisotropies, significant differences in the effective refractive indices can be obtained associated with the TE and TM modes. As a result, a device designed for the TE mode is typically not suitable for the TM mode. To improve the compatibility of integrated photonic systems, we aim to introduce the functionality for polarization control. In existing approaches for polarization rotators, two main strategies are typically employed: introducing material birefringence or structural anisotropy [74]. In our approach, material birefringence is introduced through LCs, enabling continuous polarization rotation. Specifically, reorientation of the LCs within the waveguide xy cross-sectional plane enables conversion between TE and TM polarization components, as described by Eq. (8). To accurately characterize the polarization state of the transmitted signal, we introduce four parameters: the co-/cross-polarization transmittance (T_{xx}/T_{yy} and T_{yx}/T_{xy}), the polarization rotation azimuth angle θ_p, and the ellipticity η [75]. Assuming an x-polarized wave propagates along the z-direction through the waveguide, the transmittance of the x-polarized (co-polarized) and converted y-polarized (cross-polarized) output waves are given by $T_{xx} = |t_{xx}|^2$ and $T_{yx} = |t_{yx}|^2$,

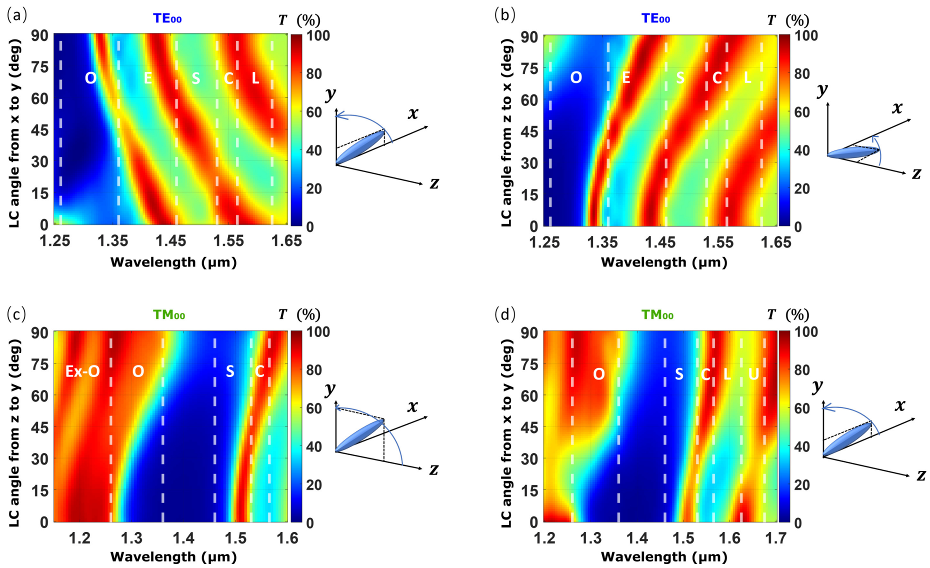
Fig. 4. Transmittances of TE_{00} and TM_{00} modes under varying LCs' orientation angles. Transmittance spectra under TE_{00} mode excitation as the LC director-field reorients from (a) the *x*-axis to the *y*-axis and (b) the *z*-axis to the *x*-axis, and under TM_{00} mode excitation as the LC director-field reorients from (c) the *z*-axis to the *y*-axis and (d) the *x*-axis to the *y*-axis.

respectively. The polarization ER is defined as the ratio between the cross- and co-polarized transmittances, expressed in decibels as $\mathrm{PER} = 10\log_{10}\left(\frac{T_{\mathrm{yx/xy}}}{T_{\mathrm{xx/yy}}}\right)$ [58,76]. At this stage, the magnitudes of the polarization components alone are insufficient to describe the polarization state accurately. It is also necessary to extract the phase information from the co- and cross polarization transmission coefficients, i.e., $\arg(t_{xx})$ and $\arg(t_{yx})$, to calculate the polarization rotation angle θ_p, which quantifies the rotation of the polarization relative to the incident wave and the ellipticity η, which characterizes the polarization type (linear, elliptical, or circular). Hence, the polarization rotation angle θ_p and the ellipticity η can be obtained from the following relations [75]:

$$\theta_p = \frac{1}{2}\tan^{-1}\left(\frac{2R\cos(\varphi)}{1-|R|^2}\right), \tag{1}$$

$$\eta = \frac{1}{2}\sin^{-1}\left(\frac{2R\sin(\varphi)}{1+|R|^2}\right), \tag{2}$$

where $R = \left|t_{yx}\right|/|t_{xx}|$ is the transmission ratio between the cross- and co-polarized components, and $\varphi = \arg(t_{yx}) - \arg(t_{xx})$ is the phase difference between the two polarization components. When $\eta = 0$, the polarization is linear. As $|\eta|$ increases, the polarization gradually transitions from linear to elliptical and eventually to circular. When $\eta \neq 0$, the sign determines the helicity of polarization: positive values for clockwise helicity and negative values for counterclockwise helicity.

We first examine the polarization control for the TE_{00} excitation. The TE_{00} can be converted to TM_{00} mode when it propagates through the structure. With LCs reorientation in the *xy*-plane, as the LCs' rotation angle approaches 45°, the polarization ER becomes high, and most of the TE mode is converted into the TM mode, as highlighted by the dashed circles in Fig. 2(a,b). When the LCs' rotation angle equals 45°, nearly complete polarization conversion is achieved. Considering the position of the passband, the operating range for polarization modulation lies within 1.4 μm to 1.55 μm, covering the E-, S-, and C-bands. In this operating range, the ellipticity of the output beam is near zero throughout all LCs' reorientation angles, as shown in Fig. 2(c), indicating that the transmitted light can be regarded as linearly polarized. Since the LCs' rotation is continuous, the proportion of the TE and TM components can be controlled, enabling synthesis of the desired linear polarization states. Consequently, the polarization rotation angle shown in Fig. 2(d) demonstrates that the device allows nearly arbitrary polarization angles. By combining the information from the ellipticity and the polarization rotation angle, it can be concluded that nearly arbitrary linear polarization states can be achieved. Similarly, under TM_{00} mode excitation, the device exhibits the same capability as the case of TE_{00} mode excitation. Within the operating range of 1.4 μm to 1.55 μm, the TM_{00} mode can also be converted into the TE_{00} mode. By continuously adjusting the LCs' rotation angle, the polarization ER between the two modes can be controlled, enabling the generation of arbitrary linear polarization states. The corresponding results are shown in Fig. 2(e–h). Overall, with the LCs reorientation strategy in the xy-plane, the polarization ER of this device reaches a maximum of 33.86 dB, with a corresponding polarization conversion efficiency of 81.86% based on the relation $P_{\text{converted}}/P_{\text{input}}$, which inherently includes the insertion loss. Accordingly, the proposed structure governed by the LCs reorientation strategies enables broadband modulation for the fundamental TE and TM modes in terms of phase, intensity, and polarization, demonstrating excellent performance.

2.3. Compact on-chip modulator enabled by 2D-Bragg structure

In the previously proposed structure, tunability is provided solely via beam propagation through the LCs medium, whereas the waveguide acts optically passive. By designing a waveguide based on a 2D-Bragg structure and optimizing it using the PSO algorithm, in addition to further mitigation of the footprint limitation, the LC-induced tunability was expanded to the overall structure. The proposed design enables a higher phase modulation of up to 1.1π for the TE_{00} mode at $\lambda = 1.55$ μm, as well as an intensity modulation at $\lambda = 1.33$ μm. For the TM_{00} mode, a phase modulation depth exceeding 1.1π over a 100 nm bandwidth at 1.21 μm and intensity modulation over a 50 nm bandwidth at $\lambda = 1.33$ μm are achieved. Furthermore, this structure is more compact, with a total length of 3.3 μm, making it promising for dense photonic integration.

In this section, the proposed structure consists of a periodic array of Si elliptical nanopillars through the top strip down to the bottom of the waveguide, as illustrated in Fig. 3(a). The empty spaces between pillars are filled with LCs. Therefore, the waveguide output can be dynamically controlled by means of tuning the LCs' alignment. Figure 3(b) presents the detailed structural parameters. The sidewalls of the etched regions are perpendicular to the substrate. The distance between the first (and last) row of nano-pillars and the LCs pool edges is $L = 310$ nm. Each elliptical pillar has a major diameter of $d_1 = 377$ nm, and the distance along the z-direction is $D_1 = 200$ nm. The minor diameter is $d_2 = 232$ nm, and the distance along the x-direction is $D_2 = 200$ nm. Figure 3(c) shows the cross-sectional view of the pillar array in the xy-plane. The exerted electrodes inducing a uniform electrostatic field horizontally (along the x-axis) are shown in yellow. The upper group of Fig. 3(h) exemplarily shows the output signal field distributions under x-aligned and z-aligned LC states during phase modulation of the TE_{00} mode at the operating wavelength of 1.55 μm. It can be observed that the TE_{00} mode maintains nearly identical field profiles under both LC orientations, with negligible mode conversion. In the lower group of Fig. 3(h), the field distributions at the operating wavelength of 1.33 μm are shown for both the on- and off-states. In the on-state, the TE_{00} mode passes through the structure with very low loss, whereas in the off-state, only a small fraction of the input light transmits. These results correspond to the green and red dashed lines in the output spectra shown in Fig. 3(d), which represent the TE_{00} mode field profiles for the respective LC states and operating wavelengths. Phase and intensity modulation of the TM_{00} mode is illustrated in Fig. 3(f), where the red and green shaded regions indicate the operating bandwidths suitable for phase and intensity modulation, respectively. The solid lines represent the total transmittance, and the dashed lines denote the TM_{00} component. Their close overlap suggests that the modulated output maintains high TM_{00} mode purity within the operating bandwidth. The corresponding phase modulation information for the TE_{00} and TM_{00} modes can be found in Fig. 3(e) and Fig. 3(g).

Since the reorientation strategy of the LCs is continuous, investigating intermediate LCs states is important. To understand how the device interacts with the fundamental TE and TM modes under intermediate LCs states, we investigated the optical responses of the device for different LCs reorientation strategies. Figure 4(a,b) shows the spectra of two LCs reorientation strategies under TE_{00} mode excitation. Unlike the above-discussed Bragg grating structure, reorienting the LCs within the *xy*-plane does not predominantly induce polarization change. Therefore, rotation of LCs within both the *xy*- and *xz*-planes can be used for phase and intensity modulation. At the wavelength of 1.33 µm, intensity modulation can be achieved by simply rotating the LCs by 45°. For phase modulation, since intensity with minimal fluctuation is observed only when the LCs' orientation angle is close to 0° or 90° around 1.43 µm and 1.55 µm, these wavelengths are suitable for implementing discrete π phase shifts.

The modulation strategies for the TM_{00} mode are shown in Fig. 4(c,d). This structure is significantly more effective for modulating the TM_{00}. As shown in Fig. 4(c), within the extended O-band, the transmittance of the TM_{00} mode remains relatively stable as the LCs are rotated in the *yz*-plane, indicating its suitability for broadband phase modulation. In contrast, within the O-band, a wide range exhibiting a high switching ratio nearly spans the entire band, making it suitable for intensity modulation. Moreover, near the telecom wavelength at 1.51 µm, we also observe the potential for intensity modulation. The other LCs modulation strategy, which rotates the LCs within the *xy*-plane, provides intensity tunability primarily within the O-band and around 1.51 µm.

3. Robustness and fabrication constraints

3.1. Fabrication imperfections

The etching strategy can impose imperfections in the fabricated structures. Here, we investigated two important types of fabrication imperfections that may impact the device's performance. First, the 1D-Bragg structure is taken as a representative design to analyze the impact of fabrication imperfections on the device performance. The performance of the 2D-Bragg structure is more sensitive to variations in structural parameters, resulting in relatively lower robustness. Therefore, the robustness analysis in this work is focused on the first design to demonstrate performance under realistic fabrication conditions.

In the above numerical study, the ideal inner sidewalls of the structure are assumed to be smooth and vertical. However, it is difficult to perfectly achieve in fabrication process. Surface imperfections introduced during the etching process can be two representative types. The first type of imperfection is the parabolic-like sidewall profile caused by focused ion beam etching, which is characterized by smooth but tilted etched surfaces due to redeposition effects [77]. The second type arises from deep reactive ion etching, where the sidewalls are generally vertical with scallop features [78]. These two imperfections are illustrated in Fig. 5(a). To investigate the impact of these two types of imperfections on the device performance, the parabolic sidewall profile and the scallop features (≈ 13.5 *textrmnm*) were introduced in the simulations. The total transmittance and mode purity of the device under TE- and TM-mode excitation were then analyzed under these imperfections.

The transmittance spectra under TE_{00} mode excitation for the three types of sidewall profiles, shown in Fig. 5(b–c), correspond to the cases where the LCs are aligned along the *x*- and *z*-directions, respectively. The solid lines indicate the total transmittance, which remains nearly unchanged by fabrication-induced structural deformations. However, the TE_{00} mode component is strongly influenced by the parabolic sidewall, resulting in reduced mode purity in the output

Optics EXPRESS

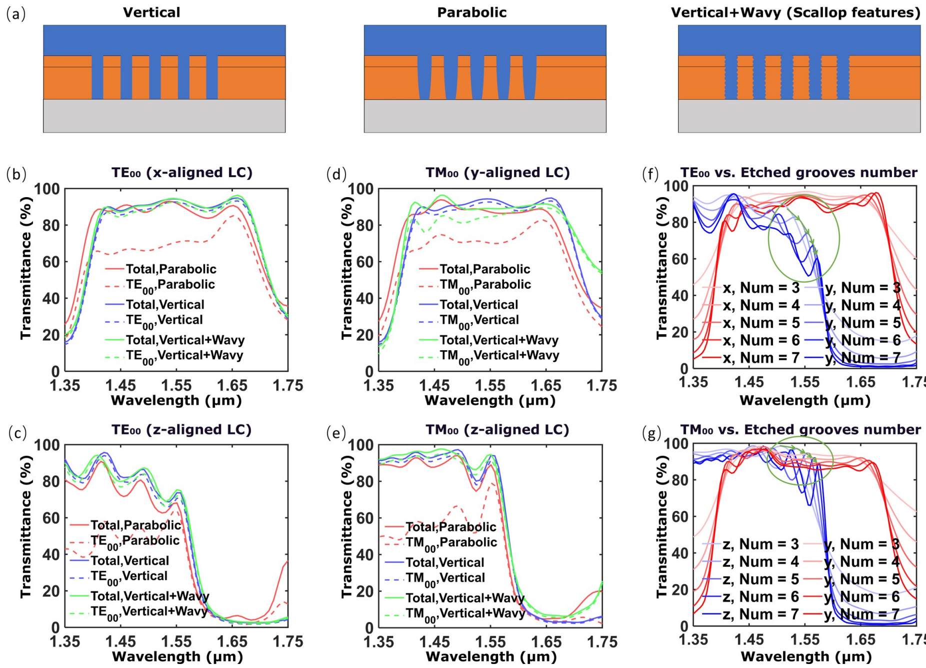

Fig. 5. Effects of fabrication imperfections and the number of etched grooves. (a) Schematic cross-sectional views of etch gratings with different sidewall profiles: vertical (left), parabolic (middle), and wavy (right). (b, c) transmittance under TE_{00} excitation for the three profiles, considering (b) x-aligned and (c) z-aligned LCs states. (d, e) transmittance under TM_{00} excitation for the three profiles, considering (d) y-aligned and (e) z-aligned LCs states. (f, g) transmittance variation under the two LCs alignment states by adjusting the number of vertical etched slits: (f) TE_{00} input, (g) TM_{00} input.

signal. For the x-aligned LC state, the transmittance peak near the photonic bandgap at 1.65 μm exhibits relatively high mode purity, which gradually degrades as the wavelength decreases. A similar trend is observed in the z-aligned state, where the peak at 1.55 μm also has high mode purity that becomes worse at shorter wavelengths. In contrast, the etched grooves fabricated using the DRIE method, which exhibit overall vertical sidewalls with scallop features, yield both total and TE_{00} mode transmittances that closely match those of the ideal structure.

Figure 5(d–e) illustrates how structural deformation modulates the TM_{00} mode under y- and z-aligned LCs states, respectively. Similar to the case of TE_{00} modulation, the parabolic sidewall features introduced by the FIB process remain the dominant factor affecting mode purity.

The phase shift arises from the change in birefringence of the LCs. As a result, increasing the number of etched grooves linearly increases the phase modulation depth. Moreover, within the photonic bandgap, reflectance is enhanced, thereby improving the optical switching ratio. This suggests that increasing the number of etched grooves without limit might seem beneficial. However, as shown in Fig. 5(f–g), the output spectra under x-/ z-aligned and y-/ z-aligned LCs for the TE_{00} and TM_{00} modes indicate that, although the number of etched grooves is increased, the intensity of the output signal at 1.55 μm drops rapidly when modulating the TE_{00} mode. This intensity degradation is highly undesirable during phase modulation. In contrast, for the TM_{00} mode, the transmittance peak near the photonic bandgap exhibits only a slight degradation. Therefore, for TM_{00} modulation, it is reasonable to consider a moderate increase in the number of etched grooves. Another reason for choosing an arbitrary number of five etched grooves is that the condition $\Gamma \approx (2N+1)\pi$ needs to be satisfied to achieve full polarization conversion. Taking

Optics EXPRESS

all these factors into account, filling five etched grooves with LCs is an appropriate choice. This configuration enables a phase modulation depth exceeding 0.92π within the operating wavelength range while maintaining a high switching ratio.

We further investigate the impact of fabrication imperfections on the 2D-Bragg structure. In the ideal case, the elliptical Si pillars are assumed to have smooth and vertical sidewalls. The tilted profile was constructed by reducing the radii at the top by 10% and increasing those at the bottom by 10%, resulting in the tilted sidewalls. The final vertical sidewall profile has scallop features on its surface, corresponding to a ±10% radial surface roughness. The transmittance spectra under TE_{00} excitation are shown in Fig. 6(a,b), corresponding to the x- and z-aligned LCs, respectively. The tilted profile introduces a noticeable deviation from the ideal vertical profile. This fabrication imperfection leads to a substantial reduction in the output mode purity. By comparison, we found that the structure with scallop features on the pillar surfaces performs nearly as well as the ideal structure. Overall, the tilted sidewall profile is the dominant fabrication imperfection that degrades device performance, whereas the scallop features have only limited impact on the total transmittance and the mode purity. To achieve optimal performance, an etching process that maintains overall vertical sidewalls remains the preferred choice, although some surface roughness, such as scallop features, is acceptable.

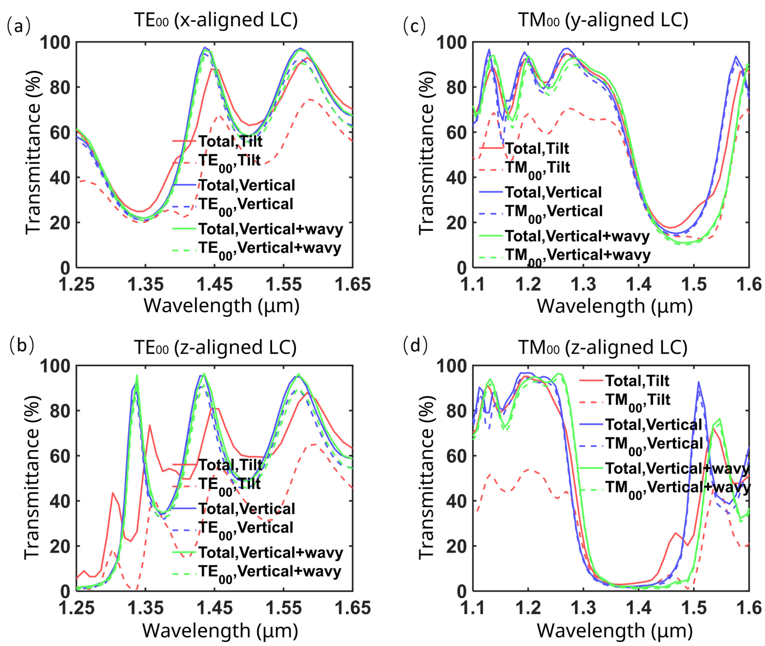

Fig. 6. Effects of fabrication imperfections in the 2D-Bragg structure. (a, b) Transmittance spectra under TE_{00} excitation for three etched pillar profiles, including tilted, vertical, and vertical sidewalls with scallop feature, considering (a) x-aligned and (b) z-aligned LC states. (c, d) Transmittance spectra under TM_{00} excitation for the three etched-pillar profiles, considering (c) y-aligned and (d) z-aligned LC states.

3.2. Optical performances under non-uniform LC director-field profiles

In the previous sections, we presented the ideal performance of the designed meta-waveguides incorporated with LCs having uniform, homogeneous alignment distributions everywhere. Here, we employed the Q-tensor approach [67–69] to obtain the actual spatially varying LC distribution, described by director-field (n_x, n_y, n_z), and to assess how realistic LC configurations affect the optical response tuning predicted by the simplified uniform-LC model. We used the commercial software COMSOL Multiphysics (v. 5.6) to calculate the LC director-field profile in the integrated structures. This was then imported into Lumerical FDTD as a spatially varying LC refractive index profile to evaluate the optical performance of each device for the practical applications. Details of the LC director-field calculation, including the employed LC materials in the studies and their properties, the LC initial alignment profile in the different designs and their associated surface anchoring conditions, and the implemented electrodes are all discussed in Sec. 4.2.

3.2.1. Polarization modulation in the 1D-Bragg structure under space-dependent LC distribution

We showed earlier that by properly defining LC orientation in the cross-sectional *xy*-plane, polarization conversion can be achieved in 1D-Bragg meta-waveguides. As discussed earlier, if the average LC alignment approaches 45° (with respect to the *y*-axis), the maximum polarization conversion can be achieved. Here, we discuss the practical LC integration and its tuning method to realize polarization conversion in such a design. Numerical modelling is performed with the assumption of a spatially dependent LC system with a positive static dielectric anisotropy. By applying voltage between laterally designed electrodes (as introduced in Fig. 1(c)), LC director-field realignment is numerically simulated employing the Q-tensor method at voltages of V = 1, 2, 3, 4, and 5 V, respectively. It is worth mentioning that the LC director-field at V = 0 V is similar to the case of V = 1 V, governed by the LC anchoring at the confining surfaces and the initial alignment. The spatially dependent director distributions were then incorporated into the optical simulation, in which mode conversion efficiency is mainly governed by the effective refractive index profile of LC inside groove domains obtained from LC alignment distributions. As shown in Fig. 7(a), for TE_{00} excitation, the strongest polarization conversion is obtained at 1 V within the operating wavelength range of 1.4–1.55 µm. As the applied voltage increases, the TE_{00} output transmittance gradually increases, corresponding to the gradually decreased TM_{00} output shown in Fig. 7(b). This indicates that the device exhibits the highest polarization conversion efficiency near the threshold voltage of about V = 1 V and the lowest conversion at the high voltages near V = 5 V and above. Therefore, dynamic tuning of the output polarization can be achieved by varying the applied voltage from 1 V up to 5 V. The TE-to-TM polarization ER of this device reaches a maximum of 25.4 dB at 1 V. A very similar polarization conversion behavior is observed for TM_{00} excitation. At 1 V, the TM_{00} mode is converted almost entirely into TE modes within the operating wavelength range, whereas at 5 V almost no polarization conversion occurs. The TM-to-TE polarization ER of this device reaches a maximum of 34.48 dB at 1 V. In Fig. 7(c, d), the LC director-field distribution is shown at the minimum (1V) and maximum (5V) applied voltages on the central cross-section of the LC-infiltrated groove within a unit cell, obtained from the Q-tensor method. As seen, by increasing the applied voltage beyond the threshold, the LC optic axis (aligned along the director-field) gradually realigns from the initial dominant alignment at $\frac{\pi}{4}$ in the groove domain and approaches the normal alignment to the substrate, hence resulting in polarization tuning.

3.2.2. Phase and intensity modulation in the 1D-Bragg structure as the function of LC spatial-dependent distribution

Intensity and phase modulation are achieved in the Groove structures within the respective operating bandwidths filled with LC with a mixed-alignment configuration (formed from all LC primarily deformations of splay, bend, and twist). In such a design, tuning is presented by varying the driving voltage that realigns the spatially distributed LC director-field. We show significant modulations of the TE_{00} and TM_{00} modes by reconfiguring LC alignment under applied voltages up to V = 7 V, where saturation occurs. We analyze the variations of the total transmittance, the transmittance of the fundamental modes, and their associated output phase, as well as the generation of the higher-order modes induced by spatially non-uniform

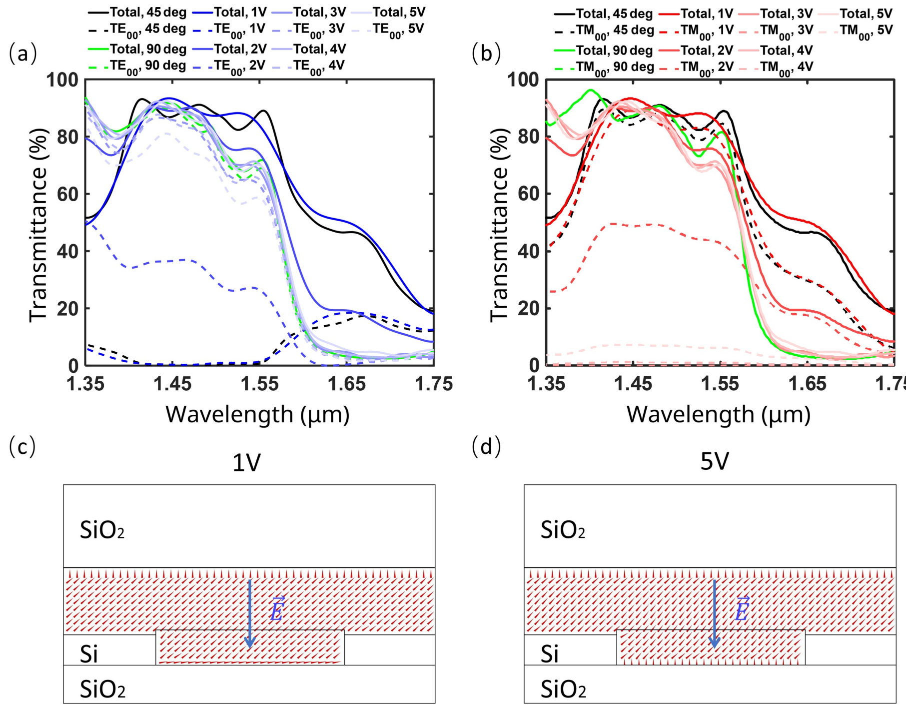

Fig. 7. Optical response and demonstration of the LC director-field distributions in the 1D-Bragg structure as a function of the applied voltage. (a, b) Transmittance spectra for TE_{00} excitation, calculated using the simulated LC director-field distributions at applied voltages of 1, 2, 3, 4, and 5 V and compared with uniform LC alignment states at 45° and 90°. For each applied voltage, the total transmittance is plotted together with the selected output mode component: (a) TE_{00} component and (b) TM_{00} component. (c, d) Cross-sectional view of the LC director-field distributions in the unit cell obtained from the Q-tensor approach at applied voltages of (c) 1 V and (d) 5 V, respectively.

LC reorientation. Figure 8(a-c) show the optical response of the device for TE_{00} excitation under different applied voltages from 1 V to 7 V, while Fig. 8(d-f) show the corresponding results for TM_{00} excitation. As shown in Fig. 8(a), the voltage tuning under the space-dependent LC distributions still preserves the photonic bandgap shift, which was reported earlier in the uniform alignment case, where the LC director-field reorients from the z-axis toward the x-axis (see Fig. 1(d)). A similar behavior is also observed in Fig. 8(d) for TM_{00} excitation when the LC reorientation takes place in the yz-plane. In comparison, the maximum photonic bandgap shifts achieved for TE and TM modes are smaller than the predicted values obtained with the assumption of a uniform, spatially independent LC director-field.

Here, space-dependent LC distribution is described by a non-uniform optical refractive index profile. As seen in Fig. 8(g,h), we also observe the formation of a 'disclination wall' at the center of the cell, thereby introducing non-negligible higher-order mode coupling channels. As seen in Fig. 8(b), modulation of the TE_{00} mode is accompanied by noticeable generation of TE_{10} component at 3 V, 5 V, and 7 V, and TE_{20} component at 1 V, 3 V, and 7 V. This leads to a decrease in the mode purity of the final output TE_{00} mode. For TM_{00} mode excitation, the higher-order mode coupling is more complex than that for TE_{00} mode excitation. As shown in Fig. 8(e), not only TM_{10} and TM_{20} components but also TE_{10} and TE_{20} components appear in the output. However, the higher-order TE components are much smaller than the higher-order TM components, in general. These findings indicate that spatially non-uniform LC reorientation

Optics EXPRESS

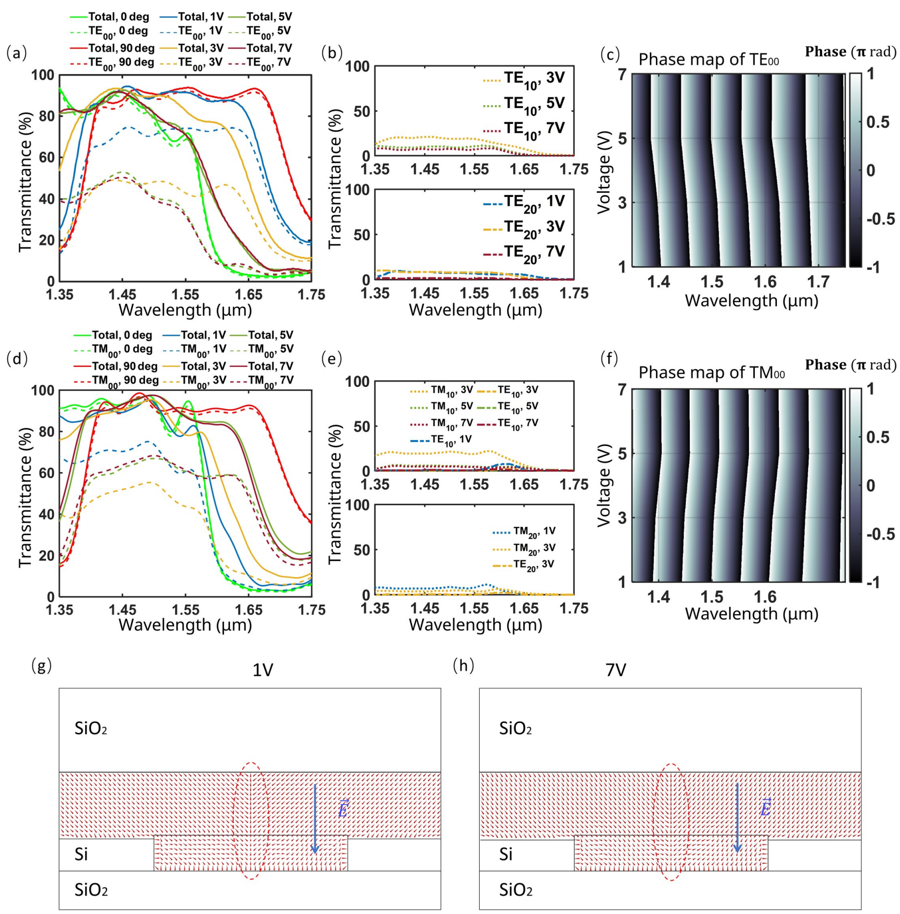

Fig. 8. Optical response tuning in the 1D-Bragg structure characterized with the LC mixed-alignment configuration under applied voltages, shown for TE_{00} mode excitation in (a–c), and for TM_{00} mode excitation in (d–f), respectively. (a) Total transmittance and TE_{00} mode transmittance. (b) Non-negligible transmittance contributions from the higher-order TE_{10} and TE_{20} modes at selected applied voltages. (c) Voltage-dependent phase map for TE_{00} excitation. (d) Total transmittance and TM_{00} mode transmittance. (e) Non-negligible transmittance contributions from the higher-order TE_{10}, TE_{20}, TM_{10}, and TM_{20} modes at selected applied voltages. (f) Voltage-dependent phase map for TM_{00} excitation. (g, h) Cross-sectional view of the LC director-field distributions in the unit cell obtained from application of the Q-tensor method at applied voltages of (g) 1 V and (h) 7 V, respectively.

can introduce both co-polarized and cross-polarized higher-order mode coupling. At 1.55 µm, increasing the applied voltage from 1 V to 7 V produces phase shifts of 0.65π and 0.57π for TE_{00} and TM_{00} excitation, respectively, as shown in Fig. 8(c) and Fig. 8(f). Compared with the uniform case (as shown in Fig. 1(f) and (i)), the optimum phase shifts of 0.92π in both fundamental TE and TM modes are slightly decreased. These results indicate that the spatial uniformity of LC reorientation is important to achieve high phase shift tuning.

3.2.3. 2D-Bragg structure with spatial-dependent LC distribution

In the 2D-Bragg structure, the device is filled with an LC material with negative dielectric anisotropy and positive, relatively high optical birefringence of 0.18 [79], where $n_o = 1.51$ and $n_e = 1.69$, to achieve a similar performance as in the idealized case reported in Sec. 2.3. The LC is driven by the uniform electrostatic field distributed along the x-axis and created between the vertically designed electrodes placed at the sides of the waveguide (as schematically shown in Fig. 3(c)). In the first defined LC configuration (as introduced in Sec. 4.2), the LC effective realignment takes place along the horizontal x-direction by reducing the in-plane rotation of the LC director-field. As seen from Fig. 9(a) and (c), the optical response profile is shifted by about 30 nm by increasing the voltage up to 10 V, and a phase modulation of 0.51π is achieved. In Fig. 9(a) and (b), the obtained results are additionally compared with the optical responses of the LC-integrated waveguide under ideal LC uniform alignments. Hence, the output modes maintain high mode purity; we only discuss the total transmittance here. In the second definition of the LC configuration described in Sec. 4.2, the average LC alignment is dominant along the normal direction to the substrate (i.e., y-axis); hence, the TM mode gets successfully tuned. In Fig. 9(b) and (d), modulation of the phase and amplitude of the TM_{00} are presented, respectively. As seen, by increasing the voltage up to 10 V, the transmittance profile is shifted by about 38 nm and a phase modulation of 0.82π is achieved. Since the pillars distort the LC distributions that modulate the guided mode within the waveguide, the application of the Q-tensor method is necessary to describe the LC system. By using this method, all the vital factors such as surface anchoring, geometrical confinement of the LC orientation distributions, and defect formation are considered.

4. Methods

4.1. Theoretical modeling of homogeneously LC-integrated Bragg gratings

Fiber Bragg gratings were previously widely applied in optical sensing and signal processing as mature all-optical components due to their low loss, low cost, and broadband operation capability [70]. They operate based on periodic perturbations of the refractive index, which induce variations in reflectance and phase. Here, we suggest tunable Bragg gratings on a silicon platform, which can be achieved, for example, by applying an etching process to create the designs and, eventually, infiltrating with LCs. As we showed earlier, by controlling the effective average LCs anisotropy in the volume surrounding the nanostructures, optical response tuning and shaping can be achieved in the metasurfaces integrated with LCs [80]. In addition, in LC-integrated metasurfaces, electrically tuned polarization and intensity are shown [30]. Relying on these tuning principles, we introduced optical response tuning in our designs.

For the phase and intensity modulation of 1D-Bragg gratings, we can perform a preliminary analysis using the transfer matrix method, which allows us to quickly establish the functional framework of the modulator before conducting 3D simulations. For a lossless symmetric system, the transfer matrix M satisfies the relation [81]:

$$M = \begin{bmatrix} \frac{1}{t^*} & \frac{r}{t} \\ \frac{r^*}{t^*} & \frac{1}{t} \end{bmatrix}, \tag{3}$$

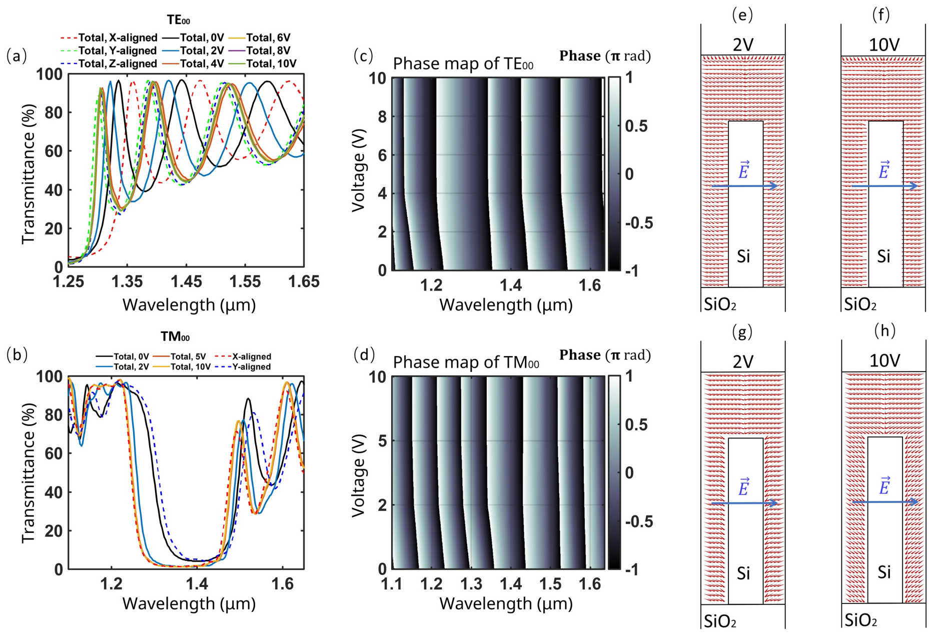

Fig. 9. Optical response of the 2D-Bragg structure under realistic voltage-dependent LC reorientation. (a, b) Transmittance spectra obtained using the simulated LC director-fields distributions at applied voltages of 0, 2, 4, 6, 8, 10 V compared with those obtained for ideal uniform LC alignment states (dashed curves): (a) TE_{00} excitation, with the *x*-, *y*-, and *z*-aligned states as references, and (b) TM_{00} excitation, with the *x*- and *y*-aligned states as references. (c, d) Corresponding phase maps as functions of wavelength and applied voltage for (c) TE_{00} and (d) TM_{00} excitation. (e–h) Cross-sectional view of the LC director-field distributions in the unit cell obtained from the Q-tensor approach at applied voltages of (e) 2 V and (f) 10 V for the first LC configuration, and (g) 2 V and (h) 10 V for the second LC configuration, respectively.

where t and r denote the complex transmission and reflectance, respectively, and t^* and r^* represent their complex conjugates. In the designed structures (introduced in Sec. 2.1), the overall transmittance $T = |t|^2$ can be derived from the M. In general, the LCs' refractive index perturbations can induce changes in both the transmittance and phase of Bragg structures embedded within the waveguide. By means of the M, the optical response tuning can be described. This method enables the description of the constructive and destructive interference in the output spectra, as well as the spectral shift. In the latter case, an increase of the effective refractive index of the LCs layer can result in a redshift of the Bragg center and vice versa. However, the M cannot describe changes in polarization state. Hence, by use of the Jones matrix method taking into account the LCs' effective birefringence, the polarization conversion can be investigated. By rotating the optical axis of the nematic LCs (with positive anisotropy) in the Cartesian coordinate system, the components of the unit director vector describing the local average alignment of LCs can be obtained from

$$n_x = \sin\theta\cos\phi, \quad n_y = \sin\theta\sin\phi, \quad n_z = \cos\theta, \tag{4}$$

where θ is the polar angle and ϕ is the azimuthal angle. If the initial director-field of the LCs is aligned along the z-axis, then the permittivity tensor can be defined as

$$\varepsilon_{\mathrm{LC}} = \begin{bmatrix} \varepsilon_{\perp} & 0 & 0 \\ 0 & \varepsilon_{\perp} & 0 \\ 0 & 0 & \varepsilon_{\parallel} \end{bmatrix}. \tag{5}$$

For any arbitrary alignment, similar to uniaxial crystalline materials [82], this can be obtained from the following relation:

$$\varepsilon_{\mathrm{LC}} = \begin{bmatrix} \varepsilon_{\perp}+\varepsilon_a n_x n_x & \varepsilon_a n_x n_y & \varepsilon_a n_x n_z \\ \varepsilon_a n_y n_x & \varepsilon_{\perp}+\varepsilon_a n_y n_y & \varepsilon_a n_y n_z \\ \varepsilon_a n_z n_x & \varepsilon_a n_z n_y & \varepsilon_{\perp}+\varepsilon_a n_z n_z \end{bmatrix}, \tag{6}$$

where $\varepsilon_a = \varepsilon_{\parallel} - \varepsilon_{\perp} = n_e^2 - n_o^2$ is the difference between the permittivities parallel and perpendicular to the director-field. Assuming that the fundamental mode injected into the Bragg grating is x-polarized with $\mathbf{E}^T = [1, 0, 0]$, the effective refractive index in the LCs-filled layer can be calculated as [83]:

$$\frac{1}{n_{\mathrm{eff}}^2} = \mathbf{E}^T \cdot \varepsilon_{\mathrm{LC}}^{-1} \cdot \mathbf{E}. \tag{7}$$

Based on the transmission coefficient t calculated from Eq. (3), the complex amplitudes of each polarization state, $E_x(\lambda)$ and $E_y(\lambda)$, can be obtained using the Jones vector:

$$E_{\mathrm{out}}(\lambda) = \begin{bmatrix} E_x(\lambda) \\ E_y(\lambda) \end{bmatrix} = \underbrace{\begin{bmatrix} \cos\phi & -\sin\phi \\ \sin\phi & \cos\phi \end{bmatrix}}_{R(\phi)} \underbrace{\begin{bmatrix} e^{-i\Gamma(\lambda)/2} & 0 \\ 0 & e^{i\Gamma(\lambda)/2} \end{bmatrix}}_{\mathrm{PD}(\Gamma)} \underbrace{\begin{bmatrix} \cos(-\phi) & -\sin(-\phi) \\ \sin(-\phi) & \cos(-\phi) \end{bmatrix}}_{R(-\phi)} \cdot \underbrace{\mathbf{t}(\lambda) \cdot \mathbf{E}^T}_{\mathbf{E}_{\mathrm{in}}(\lambda)}. \tag{8}$$

Here, the rotation matrix $R(\phi)$ and the phase delay matrix $\mathrm{PD}(\Gamma)$ are used, where $\Gamma(\lambda) = \Gamma_{90^\circ}(\lambda)$-$\Gamma_{0^\circ}(\lambda)$ represents the phase difference between the components of light polarized parallel and perpendicular to the LCs director-field after propagating through the system, which can be obtained by the previously calculated transmission coefficient t as $\arg(t)$. When $\phi = 45^\circ$, if $\Gamma \approx (2N+1)\pi$ with $N \in \mathbb{Z}$, the polarization conversion rate between x and y approaches 100%, $\mathbf{E}_{out} = [0; \mathbf{t}(\lambda); 0]$. Conversely, if $\Gamma \approx 2N\pi$, nearly no conversion occurs, $\mathbf{E}_{out} = \mathbf{E}_{in} = [\mathbf{t}(\lambda); 0; 0]$. Based on this principle, the designed 1D-Bragg grating structure enables nearly complete polarization conversion when the LCs are oriented at $\phi = 45^\circ$. We used FDTD simulations combined with optimization methods to determine and optimize the 2D-Bragg structures' performance over the targeted wavelength range. Although the phase change can be calculated using the transfer matrix method, the spectral position of the passband must also be taken into account. The passband and stopband here refer to the wavelength range where light is transmitted and blocked, respectively. When the operating wavelength range remains entirely within the passband, the device can achieve phase modulation by reorienting the LCs. In contrast, switching between the passband and the stopband can be exploited for optical switching applications. Eq (8) indicates that the polarization conversion efficiency can be evaluated in conjunction with the spectral position of the passband. Consequently, the product of the polarization conversion efficiency and the device transmittance can be used to predict the efficient spectral band for the performance of the designed structures. The introduced transfer matrix method can predict the simulation results with good accuracy. Specifically, it was found that an effective refractive index change of 0.28 can lead to a spectral shift by approximately 150 nm, while simultaneously inducing a phase shift of about π. Each LC layer (with a thickness of 424 nm) can contribute approximately 0.2π to the total accumulated phase shift, corresponding to the designed 1D-Bragg structure. The predicted polarization conversion is likewise in good agreement with the numerical simulations in Lumerical.

4.2. LC system description based on the Q-tensor method

The anisotropic, apolar LC systems are simulated using the Q-tensor approach. The Q-tensor can be described based on the unitary, pseudo-vector field, i.e., director-field $\mathbf{n}$. In the Cartesian coordinate system, the director field is given as a vector with three components (n_x, n_y, n_z). Accordingly, the Q-tensor can be described based on the director-field as [67–69]:

$$Q_{ij} = S\left(\mathbf{n} \otimes \mathbf{n} - \frac{1}{3}\delta_{ij}\right), \tag{9}$$

where S is the scalar order parameter and δ_{ij} is the Kronecker-delta function. In the waveguide designs incorporated with an LC thin film, dynamical tuning is achieved by electrically reorienting the LC. The energy stored in the LC system subjected to an electrostatic field $\mathbf{E}$ (defined as $\mathbf{E} = -\nabla V$, where V is the electric potential) can be defined as a function of the Q-tensor components as [69,84]:

$$E_E(Q_{ij}) = -\frac{1}{2}\varepsilon_0 \left(\bar{\varepsilon}\delta_{ij}(\partial_i V)(\partial_j V) + \Delta\varepsilon(\partial_j V)(\partial_k V)Q_{jk}\right), \tag{10}$$

where ε_0 is the permittivity of the free space, $\bar{\varepsilon} = \frac{1}{3}(\varepsilon_\parallel + 2\varepsilon_\perp)$ and $\Delta\varepsilon = \varepsilon_\parallel - \varepsilon_\perp$ are the LC average dielectric constant and the dielectric anisotropy, respectively, as a function of dielectric constant parallel $\varepsilon_\parallel$ and perpendicular $\varepsilon_\perp$ to the nematic director. The LC dielectric constant ε is related to the Q-tensor as $\varepsilon_{ij} = \bar{\varepsilon}\delta_{ij} + \Delta\varepsilon Q_{ij}$. To describe the LC system in a thermodynamically stable state under a quasi-static electrostatic field, the Euler–Lagrange equation is employed [85,86], defined as:

$$L\nabla^2 Q_{ij} + AQ_{ij} + B\left[(Q_{ij}Q_{ji}) - \frac{1}{3}tr(Q_{ij}Q_{ji})\delta_{ij}\right] - CQ_{ij}tr(Q_{ij}Q_{ji}) + \varepsilon_0\varepsilon_{ij}(\partial_i\Phi)(\partial_j\Phi) = 0 \tag{11}$$

where A, B and C are the material constants, and L (obtained from $L = (K_{11} + K_{33} - 2K_{22})$) [87] is the average elastic constant obtained from the Frank elastic constants K_{ii} accordingly. Studies are performed with assumption of a LC thin film with positive dielectric anisotropy, i.e., nematic LC BL009, having the static dielectric constants of $\varepsilon_\parallel = 21$ and $\varepsilon_\perp = 5.5$, and described by the Frank elastic constants of $K_{11} = 14.6$ pN, $K_{22} = 6.0$ pN, and $K_{33} = 29.9$ pN [88], respectively, and a LC thin film with negative dielectric anisotropy, i.e., nematic LC mixture (TC-002b), given $\varepsilon_\parallel = 3.45$ and $\varepsilon_\perp = 6.65$ and $K_{11} = 22$ pN, $K_{22} = 13.2$ pN, and $K_{33} = 25.7$ pN, respectively [79]. LC realignments take place at voltages above threshold ($V_{\mathrm{th}} = \pi(K_{eff}/(\epsilon_0\Delta\epsilon))^{1/2}$, where K_{eff} is the effective elastic constant being equal to K_{11} in the groove structure [89] and K_{33} [90] in the 2D-Bragg structure, respectively) of 1.0 V and 1.82 V for the nematic LC BL009 and nematic LC TC-002b, respectively. It is worth mentioning that application of LC material with larger optical birefringence and larger static dielectric anisotropy can further enhance the optical response tuning in the designed meta-waveguides.

In the first design, LC with positive dielectric anisotropy is employed. There, two different configurations are imposed to the LC profiles to achieve the desired optical tuning in the groove meta-waveguide. Parallel electrodes (shown in Fig. 1(c)) are designed laterally to induce LC (with static positive dielectric anisotropy) realignments along the normal direction to the substrate at the cross-sectional plane. In general, a similar method can be used for the LCs infiltration as reported in LC-integrated metasurfaces [29,91]. In order to achieve polarization tuning in such designs as a result of rotating the LC optic axis in the cross-sectional plane of the waveguide, LC is given a weak anchoring [86] at the bottom surface of the groove domains, being initially in the planar alignment with respect to the substrate. Meanwhile, strong LC anchoring is imposed at the top cover surface to achieve a desired uniform LC profile and its tuning in the thin film. In addition, intensity tuning is presented in the groove meta-waveguide by tuning the LC effective refractive index in response to the applied electrostatic field in the hybrid alignment. This is generated by assuming strong anchoring at all groove walls along the normal direction to each respective surface. Here, no anchoring is imposed at the LC top cover surface. By increasing the applied voltage to impose LC realignment, the optical intensity of the fundamental mode reduces significantly and conversion to higher-order modes is obtained (See Fig. 8). In such a configuration, a disclination wall [92] also forms in the middle of the LC groove cell, impacting the optical response tuning in the integrated waveguide device.

In the second design of 2D-Bragg structure, studies are performed for the LC material with negative dielectric anisotropy aiming at enhancing LC realignment in small volumes surrounding the pillars and improving the device response time. Here, investigations are performed for two different LC configurations to achieve efficient fundamental mode tuning. In the first case, LC is initially assumed in the planar alignment above pillars, having strong anchoring along the normal direction to the pillars' surfaces, and strong homeotropic alignment is imposed at the top cover surface of the LC cell (placed at y = 0.8 μm above the waveguide). In-plane average LC alignment enhances the TE_{00} mode tuning. In the second case, the LC initial alignment is defined as homeotropic inside the LC volume, and strong tangential alignment is also imposed at the pillars' surfaces, while no anchoring is imposed on the LC top cover surface to achieve maximum average LC alignment along the normal direction and its tuning under applied voltage aimed at TM_{00} mode tuning. The device is electrically addressed by introducing ITO electrodes [93] placed at the sides of the structure in the xy-plane (shown in Fig. 3(c)) having no impact on the performance of the waveguide. By increasing voltage beyond the threshold, the LC principal axis tends to get oriented perpendicular to the uniform electrostatic field [94,95], hence forming a uniform V-shaped profile in the middle of the cell above the pillars (See Fig. 9(e–h)).

In the designed structures, the response times can be estimated as [96,97],

$$\tau_{\text{rise}} \sim \frac{\tau_0}{(V/V_{\text{th}})^2 - 1}, \tag{12}$$

$$\tau_{\text{decay}} \sim \tau_0 = \frac{\gamma_1 d^2}{K_{eff}\pi^2} \tag{13}$$

where V is the applied voltage, V_{th} is the threshold voltage, γ_1 is the rotational viscosity, and d is the LC layer thickness. For the LC BL009-filled groove structure, the rise time and decay time are calculated equal to 2.67 ms and 64.19 ms, respectively, using the values of $\gamma_1 = 0.37$ Pa s [98], $d = 5$ μm, $V_{\text{th}} = 1.0$ V, and $V = 5$ V. For the LC TC-002b-filled pillar structure characterized with small LC domains surrounding pillars, the fast rise time and decay time are calculated equal to 8.8 μs and 257.5 μs, respectively, using $\gamma_1 = 0.35$ Pa s [79], $d = 0.432$ μm [97], $V_{\text{th}} = 1.82$ V, and $V = 10$ V.

5. Conclusions

In this work, we proposed and numerically investigated two types of LC-integrated nanostructured waveguides based on 1D- and 2D-Bragg grating structures. Initial investigations were performed by modeling the LC as a spatially uniform anisotropic medium and analyzing the resulting meta-waveguides using the transfer matrix method and full-wave simulations. While this approach can provide an insightful framework for device design and performance estimation, its applicability to experimentally realistic LC-infiltrated meta-waveguides must be assessed. As a result, we conducted a comprehensive study using spatially varying LC distributions within and above the waveguide structures. The LC initial configurations and their voltage-induced reorientation were simulated using the Q-tensor approach accounting for bulk elastic deformations, surface anchoring effects, and electrode-induced reorientation. LCs with both positive and negative dielectric anisotropy were employed together with appropriately designed planar electrode configurations to realize the targeted optical response in each structure. This analysis enabled identification of the realistic LCs director-field distributions and their infiltration conditions into each device that can eventually provide the desired optical tuning functionalities approaching those suggested by the application of the simplified uniform-LC models.

The 1D-Bragg structured modulator exhibits distinctive modulation capabilities in terms of intensity, phase, and polarization within a compact footprint of 4.3 µm × 10 µm. As an optical switch, it can achieve extinction ratios of 14.6 dB (TE_{00}) and 13.8 dB (TM_{00}) at 1.65 µm with low insertion loss. As a phase modulator, it provides approximately π phase shifts for both TE_{00} and TM_{00} modes in the 1.4 µm to 1.55 µm range, accompanied by relatively small intensity variations, corresponding to a $V_\pi L_\pi$ value of $V_\pi \times 4.67$ µm. In addition, when operating as a polarization converter, it can achieve a high polarization extinction ratio of up to 33.86 dB at 1.46 µm, exceeding the polarization ER values of previously reported passive devices. Furthermore, by tuning the LCs orientation, arbitrary linear polarization states can be observed at the output port.

The proposed LC-integrated 2D-Bragg structured modulator further improves compactness, with a footprint of only 3.3 µm × 10 µm. It enables phase and intensity modulation in the low-dispersion spectral region around 1.3 µm, offering low-loss 0–π phase tuning and high-contrast intensity control for both the fundamental TE and TM modes. As a phase modulator, it exhibits a $V_\pi L_\pi$ value of $V_\pi \times 3$ µm. When operating as an optical switch, it achieves extinction ratios of 5.89 dB (TE) and 14.5 dB (TM). Overall, the LC-integrated Bragg-structured waveguides provide broadband, continuous, and efficient modulation of intensity, phase, and polarization within ultra-compact footprints. Their reconfigurability, multifunctionality, and ultra-compact footprints make them promising building blocks for densely integrated and dynamically programmable photonic circuits.

Funding. Leibniz Young Investigator Grants program by Leibniz University Hannover (YIG-2023-04); Deutsche Forschungsgemeinschaft (DFG, German Research Foundation) under Germany's Excellence Strategy within the Cluster of Excellence PhoenixD (EXC 2122, Project ID 390833453); DFG Research Grant (CA 2763/6-1, ID 544158178).

Disclosures. The authors declare no competing financial interests.

Author Contributions. W.X. and A.H. performed the numerical studies and wrote the original draft. A.H. and A.C.L. equally co-supervised the research work and secured the funding. All authors discussed the results and contributed to writing the manuscript.

Data availability. The data underlying all figures presented in this work are publicly available.

References

1. A. Karabchevsky, A. Katiyi, A. S. Ang, *et al.*, "On-chip nanophotonics and future challenges," Nanophotonics **9**(12), 3733–3753 (2020).
2. H. Huang, A. C. Overvig, Y. Xu, *et al.*, "Leaky-wave metasurfaces for integrated photonics," Nat. Nanotechnol. **18**(6), 580–588 (2023).
3. Y. Yang, J. Seong, M. Choi, *et al.*, "Integrated metasurfaces for re-envisioning a near-future disruptive optical platform," Light: Sci. Appl. **12**(1), 152 (2023).
4. P. Cheben, R. Halir, J. H. Schmid, *et al.*, "Subwavelength integrated photonics," Nature **560**(7720), 565–572 (2018).
5. L. Sun, Y. Zhang, Y. He, *et al.*, "Subwavelength structured silicon waveguides and photonic devices," Nanophotonics **9**(6), 1321–1340 (2020).
6. P. Cheben, J. H. Schmid, R. Halir, *et al.*, "Recent advances in metamaterial integrated photonics," Adv. Opt. Photonics **15**(4), 1033 (2023).
7. Z. Li, M.-H. Kim, C. Wang, *et al.*, "Controlling propagation and coupling of waveguide modes using phase-gradient metasurfaces," Nat. Nanotechnol. **12**(7), 675–683 (2017).
8. E. Falek, A. Katiyi, Y. Greenberg, *et al.*, "On-chip metasurface-on-facets for ultra-high transmission through waveguides in near-infrared," Adv. Opt. Mater. **9**(11), 2100130 (2021).

9. G. Roberts, C. Ballew, T. Zheng, *et al.*, "3d-patterned inverse-designed mid-infrared metaoptics," Nat. Commun. **14**(1), 2768 (2023).
10. Y. Meng, Y. Chen, L. Lu, *et al.*, "Optical meta-waveguides for integrated photonics and beyond," Light: Sci. Appl. **10**(1), 235 (2021).
11. A. Sabatti, J. Kellner, F. Kaufmann, *et al.*, "Extremely high extinction ratio electro-optic modulator via frequency upconversion to visible wavelengths," Opt. Lett. **49**(14), 3870 (2024).
12. W. Wang, X. Yu, S. Lai, *et al.*, "Optically-reconfigurable integrated optical directed logic computing based on silicon photonics," Opt. Express **32**(14), 24007 (2024).
13. H. Iyer and Y. Vlasov, "Ultra-high numerical aperture waveguide-integrated meta beam shaper," Optica **11**(12), 1750–1761 (2024).
14. Y. Kan and S. I. Bozhevolnyi, "Advances in metaphotonics empowered single photon emission," Adv. Opt. Mater. **11**(10), 2202759 (2023).
15. H. Zhou, J. Dong, J. Cheng, *et al.*, "Photonic matrix multiplication lights up photonic accelerator and beyond," Light: Sci. Appl. **11**(1), 30 (2022).
16. W. Liu, M. Li, R. S. Guzzon, *et al.*, "A fully reconfigurable photonic integrated signal processor," Nat. Photonics **10**(3), 190–195 (2016).
17. Z. Xu, B. Tang, X. Zhang, *et al.*, "Reconfigurable nonlinear photonic activation function for photonic neural network based on non-volatile opto-resistive ram switch," Light: Sci. Appl. **11**(1), 288 (2022).
18. J. Yu, Z. Liu, M. Wang, *et al.*, "Strain-enabled phase transition of periodic metasurfaces," Adv. Mater. **34**(1), 2102560 (2022).
19. S. Abdollahramezani, O. Hemmatyar, M. Taghinejad, *et al.*, "Electrically driven reprogrammable phase-change metasurface reaching 80% efficiency," Nat. Commun. **13**(1), 1696 (2022).
20. D.-Q. Zhang, G.-M. Pan, Z.-W. Jin, *et al.*, "Tunable dielectric metasurfaces by structuring the phase-change material," Opt. Express **30**(3), 4312–4326 (2022).
21. G. Sinatkas, T. Christopoulos, O. Tsilipakos, *et al.*, "Electro-optic modulation in integrated photonics," J. Appl. Phys. **130**(1), 010901 (2021).
22. A. Komar, R. Paniagua-Domínguez, A. Miroshnichenko, *et al.*, "Dynamic beam switching by liquid crystal tunable dielectric metasurfaces," ACS Photonics **5**(5), 1742–1748 (2018).
23. E. Melnikova, Y. Pantsialeyeva, D. Gorbach, *et al.*, "Tunable liquid crystal twisted-planar fresnel lens for vortex topology determination," Laser Photonics Rev. **19**(4), 2401006 (2025).
24. Y. V. Izdebskaya, Z. Yang, M. Liu, *et al.*, "Magnetic tuning of liquid crystal dielectric metasurfaces," Nanophotonics **11**(17), 3895–3900 (2022).
25. M. Sharma, L. Michaeli, D. B. Haim, *et al.*, "Liquid crystal switchable surface lattice resonances in plasmonic metasurfaces," ACS Photonics **9**(8), 2702–2712 (2022).
26. D. Kang, H. Heo, Y. Yang, *et al.*, "Liquid crystal-integrated metasurfaces for an active photonic platform," Opto-Electron. Adv. **7**(6), 230216 (2024).
27. L.-Y. Chiang, C.-T. Wang, S. Pappert, *et al.*, "Silicon–organic hybrid thermo-optic switch based on a slot waveguide directional coupler," Opt. Lett. **47**(15), 3940–3943 (2022).
28. L.-Y. Chiang, C.-T. Wang, S. Pappert, *et al.*, "Ultralow-v π l silicon electro-optic directional coupler switch with a liquid crystal cladding," IEEE Photonics Technol. Lett. **33**(15), 796–799 (2021).
29. M. Parry, A. Komar, B. Hopkins, *et al.*, "Active tuning of high-q dielectric metasurfaces," Appl. Phys. Lett. **111**(5), 053102 (2017).
30. Y. Hu, X. Ou, T. Zeng, *et al.*, "Electrically tunable multifunctional polarization-dependent metasurfaces integrated with liquid crystals in the visible region," Nano Lett. **21**(11), 4554–4562 (2021).
31. B. Gao, M. Ren, W. Wu, *et al.*, "Lithium niobate metasurfaces," Laser Photonics Rev. **13**(5), 1800312 (2019).
32. G. Yang, A. V. Sergienko, and A. Ndao, "Tunable polarization mode conversion using thin-film lithium niobate ridge waveguide," Opt. Express **29**(12), 18565–18571 (2021).
33. C. Wang, M. Zhang, X. Chen, *et al.*, "Integrated lithium niobate electro-optic modulators operating at cmos-compatible voltages," Nature **562**(7725), 101–104 (2018).
34. Y. Shuto and M. Amano, "Reflection measurement technique of electro-optic coefficients in lithium niobate crystals and poled polymer films," J. Appl. Phys. **77**(9), 4632–4638 (1995).
35. H. Han, J. Wang, Z. Wang, *et al.*, "Integrated barium titanate electro-optic modulators operating at cmos-compatible voltage," Appl. Opt. **62**(22), 6053–6059 (2023).
36. P. Steglich, C. Villringer, B. Dietzel, *et al.*, "On-chip dispersion measurement of the quadratic electro-optic effect in nonlinear optical polymers using a photonic integrated circuit technology," IEEE Photonics J. **11**(3), 1–10 (2019).
37. A. Rahim, A. Hermans, B. Wohlfeil, *et al.*, "Taking silicon photonics modulators to a higher performance level: state-of-the-art and a review of new technologies," Adv. Photonics **3**(02), 024003 (2021).
38. M. Shabaninezhad, H. Mehrvar, E. Bernier, *et al.*, "Plasmonic electro-optic modulators based on epsilon-near-zero materials: comparing the classical drift-diffusion and schrodinger-poisson coupling models," Opt. Express **33**(3), 4474–4490 (2025).
39. A. Karabchevsky, A. Hazan, and A. Dubavik, "All-optical polarization-controlled nanosensor switch based on guided-wave surface plasmon resonance via molecular overtone excitations in the near-infrared," Adv. Opt. Mater. **8**(19), 2000769 (2020).

40. B. Sun, F. Morozko, P. S. Salter, *et al.*, "On-chip beam rotators, adiabatic mode converters, and waveplates through low-loss waveguides with variable cross-sections," Light: Sci. Appl. **11**(1), 214 (2022).
41. F. Morozko, A. Novitsky, A. Mikhalychev, *et al.*, "On-chip polarization-encoded single-qubit gates with twisted waveguides," Phys. Rev. Res. **5**(4), 043155 (2023).
42. Y. D. Sırmacı, A. Barreda Gomez, T. Pertsch, *et al.*, "All-dielectric huygens' meta-waveguides for resonant integrated photonics," Laser Photonics Rev. **17**(6), 2200860 (2023).
43. H. Sun, Q. Qiao, Q. Guan, *et al.*, "Silicon photonic phase shifters and their applications: A review," Micromachines **13**(9), 1509 (2022).
44. Y. Kim, J.-H. Han, D. Ahn, *et al.*, "Heterogeneously-integrated optical phase shifters for next-generation modulators and switches on a silicon photonics platform: A review," Micromachines **12**(6), 625 (2021).
45. S. Liu, J. Feng, Y. Tian, *et al.*, "Thermo-optic phase shifters based on silicon-on-insulator platform: state-of-the-art and a review," Front. Optoelectron. **15**(1), 9 (2022).
46. G. M. Rebeiz, G.-L. Tan, and J. S. Hayden, "Rf mems phase shifters: Design and applications," IEEE Microwave **3**(2), 72–81 (2002).
47. T. Grottke, W. Hartmann, C. Schuck, *et al.*, "Optoelectromechanical phase shifter with low insertion loss and a 13π tuning range," Opt. Express **29**(4), 5525–5537 (2021).
48. M. Jacques, A. Samani, E. El-Fiky, *et al.*, "Optimization of thermo-optic phase-shifter design and mitigation of thermal crosstalk on the soi platform," Opt. Express **27**(8), 10456–10471 (2019).
49. P. Dong, L. Chen, and Y.-k. Chen, "High-speed low-voltage single-drive push-pull silicon mach-zehnder modulators," Opt. Express **20**(6), 6163–6169 (2012).
50. S. Liu, X. Yang, L. Lu, *et al.*, "Phase-change material enabled silicon phase shifter actuated by a highly durable graphene microheater," J. Opt. Microsyst. **4**(03), 031207 (2024).
51. X. Tu, C. Song, T. Huang, *et al.*, "State of the art and perspectives on silicon photonic switches," Micromachines **10**(1), 51 (2019).
52. X. Chen, J. Lin, and K. Wang, "A review of silicon-based integrated optical switches," Laser Photonics Rev. **17**(4), 2200571 (2023).
53. X. Luo, J. Song, S. Feng, *et al.*, "Silicon high-order coupled-microring-based electro-optical switches for on-chip optical interconnects," IEEE Photonics Technol. Lett. **24**(10), 821–823 (2012).
54. T. Kita and M. Mendez-Astudillo, "Ultrafast silicon mzi optical switch with periodic electrodes and integrated heat sink," J. Lightwave Technol. **39**(15), 5054–5060 (2021).
55. Y. Huang, Q. Cheng, Y.-H. Hung, *et al.*, "Multi-stage 8$\times$ 8 silicon photonic switch based on dual-microring switching elements," J. Lightwave Technol. **38**(2), 194–201 (2019).
56. J. Wang, J. Xiao, and X. Sun, "Design of a broadband polarization rotator for silicon-based cross-slot waveguides," Appl. Opt. **54**(12), 3805–3810 (2015).
57. J. E. Villegas, S. R. Tamalampudi, and M. Rasras, "High-speed polarization control in integrated silicon photonics," Opt. Express **33**(8), 18477–18491 (2025).
58. H. Zhang, S. Das, J. Zhang, *et al.*, "Efficient and broadband polarization rotator using horizontal slot waveguide for silicon photonics," Appl. Phys. Lett. **101**(2), 021105 (2012).
59. S. Asadulina, A. Bogdanov, and O. Yermakov, "All-dielectric meta-waveguides for flexible polarization control of guided light," Laser Photonics Rev. **18**(12), 2300544 (2024).
60. X. He, Y. Xu, B. Zhang, *et al.*, "Highly efficient and tunable polarization rotator based on lithium niobate on an insulator," Appl. Opt. **62**(10), 2434–2441 (2023).
61. M. W. Pruessner, N. F. Tyndall, and T. H. Stievater, "Mems-tunable polarization management in photonic integrated circuits," Opt. Express **31**(19), 31316–31328 (2023).
62. C. Jung, E. Lee, and J. Rho, "The rise of electrically tunable metasurfaces," Sci. Adv. **10**(34), eado8964 (2024).
63. Y. Ma, Y. Shan, Y. Cheng, *et al.*, "The birefringence and extinction coefficient of ferroelectric liquid crystals in the terahertz range," in *Photonics*, vol. 10 (MDPI, 2023), p. 1368.
64. V. Borshch, S. V. Shiyanovskii, and O. D. Lavrentovich, "Nanosecond electro-optic switching of a liquid crystal," Phys. Rev. Lett. **111**(10), 107802 (2013).
65. C. Dong, Z. Zhou, X. Gu, *et al.*, "Dynamic spectral modulation on meta-waveguides utilizing liquid crystal," Adv. Sci. **10**(34), 2304116 (2023).
66. C. Dong, X. Gu, Y. He, *et al.*, "An ultra-compact integrated phase shifter via electrically tunable meta-waveguides," Nanoscale Horiz. **10**(5), 933–943 (2025).
67. F. Bisi, E. C. Gartland Jr, R. Rosso, *et al.*, "Order reconstruction in frustrated nematic twist cells," Phys. Rev. E **68**(2), 021707 (2003).
68. A. Habibpourmoghadam, L. Jiao, V. Reshetnyak, *et al.*, "Optical manipulation and defect creation in a liquid crystal on a photoresponsive surface," Phys. Rev. E **96**(2), 022701 (2017).
69. G.-D. Lee, P. J. Bos, S. H. Ahn, *et al.*, "Fast q-tensor method for modeling the dynamics of defects in a liquid crystal director field," Phys. Rev. E **67**(4), 041715 (2003).
70. A. Lininger, A. Y. Zhu, J.-S. Park, *et al.*, "Optical properties of metasurfaces infiltrated with liquid crystals," Proc. Natl. Acad. Sci. **117**(34), 20390–20396 (2020).
71. G. T. Reed, G. Mashanovich, F. Y. Gardes, *et al.*, "Silicon optical modulators," Nat. Photonics **4**(8), 518–526 (2010).

72. B. J. Puttnam, R. S. Luís, I. Phillips, *et al.*, "High data-rate oesclu-band transmission," J. Lightwave Technol. **43**(23), 10371–10379 (2025).
73. A. Ferrari, A. Napoli, J. K. Fischer, *et al.*, "Assessment on the achievable throughput of multi-band itu-t g. 652. d fiber transmission systems," J. Lightwave Technol. **38**(16), 4279–4291 (2020).
74. H. Zafar and M. F. Pereira, "Recent progress in light polarization control schemes for silicon integrated photonics," Laser Photonics Rev. **18**(11), 2301025 (2024).
75. F.-y. Yu, Q.-c. Wang, M.-x. He, *et al.*, "Actively switchable polarization converter for reflection and transmission in the same terahertz frequencies," Eur. Phys. J. D **77**(5), 82 (2023).
76. G. Cheng, Q. Yi, Z. Yan, *et al.*, "Ultrahigh-extinction-ratio and broadband all-silicon tm-pass polarizer by employing multimode anti-symmetric apodized bragg grating," APL Photonics **8**(4), 046112 (2023).
77. W. C. Hopman, F. Ay, W. Hu, *et al.*, "Focused ion beam scan routine, dwell time and dose optimizations for submicrometre period planar photonic crystal components and stamps in silicon," Nanotechnology **18**(19), 195305 (2007).
78. O. Fursenko, J. Bauer, S. Marschmeyer, *et al.*, "Through silicon via profile metrology of bosch etching process based on spectroscopic reflectometry," Microelectron. Eng. **139**, 70–75 (2015).
79. S. Gauza, P. Kula, X. Liang, *et al.*, "High birefringence and low viscosity liquid crystals with negative dielectric anisotropy," Mol. Cryst. Liq. Cryst. **509**(1), 47/[789]–59/[801] (2009).
80. A. Habibpourmoghadam, B. N. Chichkov, and A. Calà Lesina, "Optical self-tuning of ferroelectric metasurfaces infiltrated with nematic liquid crystals via photovoltaic effect," Adv. Opt. Mater. **13**(20), 2500532 (2025).
81. B. E. A. Saleh and M. C. Teich, *Fundamentals of Photonics*, 2nd Edition (John Wiley & Sons, 2019). Chapter 7.
82. A. Habibpourmoghadam, W. Xie, P. Bessel, *et al.*, "Numerical modeling of transient absorption in hybrid dual-plasmonic au/cus nanocrystals," J. Phys. Chem. C **128**(49), 21237–21244 (2024).
83. M. Born and E. Wolf, *Principles of optics: electromagnetic theory of propagation, interference and diffraction of light* (Elsevier, 2013).
84. H. Mori, E. C. Gartland Jr, J. R. Kelly, *et al.*, "Multidimensional director modeling using the q tensor representation in a liquid crystal cell and its application to the π cell with patterned electrodes," Jpn. J. Appl. Phys. **38**(1R), 135 (1999).
85. O. M. Tovkach, C. Conklin, M. C. Calderer, *et al.*, "Q-tensor model for electrokinetics in nematic liquid crystals," Phys. Rev. Fluids **2**(5), 053302 (2017).
86. A. Habibpourmoghadam, "Electro-optically induced responses and diffractive effects in liquid crystal cells: investigating experiments and simulations," Doctoral dissertation, Otto-von-Guericke-Universität Magdeburg, Magdeburg, Germany (2021).
87. R. Soref, "Field effects in nematic liquid crystals obtained with interdigital electrodes," J. Appl. Phys. **45**(12), 5466–5468 (1974).
88. T. Kraan, T. Van Bommel, and R. Hikmet, "Modeling liquid-crystal gradient-index lenses," J. Opt. Soc. Am. A **24**(11), 3467–3477 (2007).
89. M. Sluijter, D. De Boer, and H. Urbach, "Simulations of a liquid-crystal-based electro-optical switch," Opt. Lett. **34**(1), 94–96 (2009).
90. M. Ohtsu, T. Akahane, and T. Tako, "Birefringence of n-type nematic liquid crystals due to electrically induced deformations of vertical alignment," Jpn. J. Appl. Phys. **13**(4), 621–629 (1974).
91. A. Komar, Z. Fang, J. Bohn, *et al.*, "Electrically tunable all-dielectric optical metasurfaces based on liquid crystals," Appl. Phys. Lett. **110**(7), 071109 (2017).
92. A. de Lózar, W. Schöpf, I. Rehberg, *et al.*, "Transformation from walls to disclination lines: Statics and dynamics of the pincement transition," Phys. Rev. E:Stat., Nonlinear, Soft Matter Phys. **72**(5), 051713 (2005).
93. A. Habibpourmoghadam, "Photorefractive effect in nlc cells caused by anomalous electrical properties of ito electrodes," Crystals **10**(10), 900 (2020).
94. H. Xianyu, Q. Song, S. Gauza, *et al.*, "12.2: Large negative dielectric anisotropy and high-birefringence liquid crystals," in *SID Symposium Digest of Technical Papers*, vol. 38 (Wiley Online Library, 2007), pp. 146–149.
95. A. Habibpourmoghadam, "Theoretical prediction of umbilics creation in nematic liquid crystals with positive dielectric anisotropy," ACS Omega **4**(25), 21459–21468 (2019).
96. R. Dąbrowski, P. Kula, and J. Herman, "High birefringence liquid crystals," Crystals **3**(3), 443–482 (2013).
97. J. Sun and S.-T. Wu, "Recent advances in polymer network liquid crystal spatial light modulators," J. Polym. Sci., Part B:Polym. Phys. **52**(3), 183–192 (2014).
98. E.-A. Dorjgotov, "Tunable liquid crystal etalon and photonic devices," Ph.D. thesis, Kent State University (2010).